Facile Approach to Prepare Porous CaSnO$_3$ Nanotubes via a Single Spinneret Electrospinning Technique as Anodes for Lithium Ion Batteries

Linlin Li,[†,#] Shengjie Peng,[†] Jin Wang,[†] Yan Ling Cheah,[†] Peifen Teh,[†] Yahwen Ko,[†] Chuiling Wong,[†] and Madhavi Srinivasan*[†,#]

[†]School of Materials Science and Engineering, Nanyang Technological University, 50 Nanyang Avenue, Singapore, 639798
[#]TUM-CREATE Center for Electromobility, Nanyang Technological University, 62 Nanyang Drive, Singapore 637459

S Supporting Information

ABSTRACT: CaSnO$_3$ nanotubes are successfully prepared by a single spinneret electrospinning technique. The characterized results indicate that the well-crystallized one-dimensional (1D) CaSnO$_3$ nanostructures consist of about 10 nm nanocrystals, which interconnect to form nanofibers, nanotubes, and ruptured nanobelts after calcination. The diameter and wall thickness of CaSnO$_3$ nanotubes are about 180 and 40 nm, respectively. It is demonstrated that CaSnO$_3$ nanofiber, nanotubes, and ruptured nanobelts can be obtained by adjusting the calcination temperature in the range of 600–800 °C. The effect of calcination temperature on the morphologies of electrospun 1D CaSnO$_3$ nanostructures and the formation mechanism leading to 1D CaSnO$_3$ nanostructures are investigated. As anodes for lithium ion batteries, CaSnO$_3$ nanotubes exhibit superior electrochemical performance and deliver 1168 mAh g^{-1} of initial discharge capacity and 565 mAh g^{-1} of discharge capacity up to the 50th cycle, which is ascribed to the hollow interior structure of 1D CaSnO$_3$ nanotubes. Such porous nanotubular structure provides both buffer spaces for volume change during charging/discharging and rapid lithium ion transport, resulting in excellent electrochemical performance.

KEYWORDS: CaSnO$_3$ nanotubes, CaSnO$_3$ nanofibers, electrospinning, lithium ion batteries, anodes, electrochemical performance
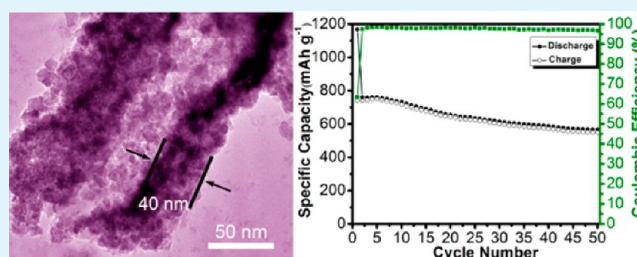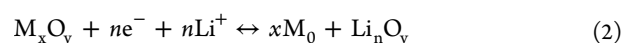
1. INTRODUCTION

Lithium ion batteries (LIBs), as a versatile power source, have been widely used in various portable electronic devices. With the development of advanced technologies, research focus is on high energy LIBs[1,2] that are suitable for applications in electric vehicles (EVs), hybrid electric vehicles (HEVs), and plug-in hybrid electric vehicles (PHEVs). Such applications ideally require LIBs of high energy density, high power, good cycling performance, excellent safety, thermal stability, low cost, and low toxicity. To achieve high energy density, novel materials are required to replace presently used graphite anodes (theoretical specific capacity 372 mAh g^{-1}). Currently, various transition metal oxides (TMOs) have been extensively studied as promising LIBs anode substitutes due to their high theoretical capacity (~400–900 mAh g^{-1}).[3] These metal oxides react with lithium via two main approaches:

Alloying/dealloying reaction,

$$MO + 2Li \rightarrow M + Li_2O \quad \text{and}$$

$$M + xLi^+ + xe^- \leftrightarrow Li_xM \tag{1}$$
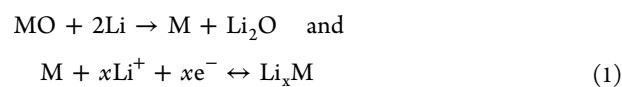
Conversion reaction,

$$M_xO_y + ne^- + nLi^+ \leftrightarrow xM_0 + Li_nO_y \tag{2}$$

Among various TMOs, Sn-based binary and ternary oxides[4−9] are particularly attractive alternatives to graphite anodes, owing to their improved safety and high theoretical reversible capacity (782 mAh g^{-1}) at a lower potential versus Li, which is more than twice that of currently used graphite (372 mAh g^{-1}). Unfortunately, the main hindrance against commercial use of Sn-based anode materials in LIBs is the poor capacity retention over extended charge–discharge cycling. This problem mainly originates from the large, uneven volume changes (~300%) that take place upon lithium insertion and extraction within Sn-based oxides, ultimately resulting in cracking and pulverization of the grains leading to loss of contact between individual grains.[10,11] To alleviate this problem, one of the promising ways is to form Tin-based composite oxides (TCO) in which the homogeneous electrochemically active/inactive matrixes like MO$_x$ and carbon may accommodate the volume change and inhibit the aggregation.[12−15]

Hence, a series of stannates such as M$_2$SnO$_4$ (M = Zn, Mg, Mn, Co, Ca),[16−20] ASnO$_3$ (A = Ca, Sr, Ba, Co, Cd),[21−30] and

$K(M,Sn)_8O_{16}$ (M = Li, Mg, Mn, Fe) have attracted more and more attention, owing to their high lithium storage capacity and relieving the volume change during cycling, which is attributed to the formation of electrochemical active/inactive MO_x matrix occurring during the first discharge process. Recently, intensive research has been carried out on M_2SnO_4-based (Zn_2SnO_4, Mn_2SnO_4, Co_2SnO_4)[16−20] and $ASnO_3$-based anodes ($CaSnO_3$, $CoSnO_3$, $SrSnO_3$).[21−30] By keeping this in mind, among various matrix elements studied in conjunction with Sn oxides, electrochemically inactive matrix element Ca was considered as a good candidate. Although $CaSnO_3$ has been prepared by sol−gel, hydrothermal, and solid-state methods, all of these measured $CaSnO_3$ electrodes lie in a relatively small voltage window, such as 0.005−1.0 V or 0.005−1.3 V. Furthermore, it has been reported that the operating voltage plays an important effect on the reversibility of Sn-based oxide compounds.[10,24] Hence, the scope exists to improve the electrochemical performance of $CaSnO_3$ electrode in a wider large voltage window. As specially tailored morphologies could significantly enhance the electrochemical properties, it is crucial to fabricate novel $CaSnO_3$ morphologies through efficient and reliable synthesis routes to improve the electrochemical performance.

It is well-known that the electrochemical performance of anode materials is highly dependent on their diverse morphologies, sizes, and nanostructures.[31−34] The previous reports identified the importance of one-dimensional (1D) nanostructure, such as nanotubes, nanowires, nanofibers, and nanobelts, as functional materials for potential applications in many areas. To serve as anodes for LIBs, 1D nanostructured materials have many advantages due to shortened Li-ion insertion/extraction distance, facile strain relaxation upon electrochemical cycling, and large surface to volume ratio, resulting in improved capacity and cycle life of LIBs.[35,36] Hence, a large number of 1D nanostructure synthesis methods have been proposed. Among these, electrospinning, as a remarkably simple and versatile technique for preparing well-defined 1D nanostructured materials with diameters ranging from a few hundred micrometers to several nanometers, has been widely used to fabricate many anode materials for LIBs.[37] Therefore, 1D $CaSnO_3$ nanostructures with different morphologies could be achieved by varying the electrospining parameters.

To the best of our knowledge, there are few reports of the synthesis of nanostructured $CaSnO_3$ by electrospinning[38] and the application as anode materials for LIBs. In the present work, we successfully prepared $CaSnO_3$ nanotubes by a simple single-spinneret electrospinning technique. The effect of calcination temperature on the phase, morphology, micro-structure, and electrical properties of $CaSnO_3$ has been investigated. The formation mechanism of $CaSnO_3$ nano-fibers/nanotubes is proposed. As compared to nanofibers and ruptured nanobelts, elelctrospun $CaSnO_3$ nanotubes show a higher initial reversible capacity of 759 mAh g^{-1} and excellent cyclability, owing to the void interior space of nanotubes, which could accommodate the huge volume changes during cycling and facilitate the lithium ion diffusion and electrolyte penetration. Hence, the as-prepared electrospun $CaSnO_3$ nanotube exhibits improved electrochemical properties indicating its potential as an LIB anode.

2. EXPERIMENTAL SECTION

2.1. Synthesis of $CaSnO_3$. All chemical reagents were used as received. In a typical preparation of precursor solutions, first, poly (vinylpyrolidone) (PVP; Fluka) of molecular weight 360 000 was dissolved in 5 mL of absolute ethanol (Sigma Aldrich) with vigorous stirring to form a 20 wt % solution. Meanwhile, stoichiometric amounts of $SnCl_2 \cdot 2H_2O$ (Sigma Aldrich) and $Ca(NO_3)_2 \cdot 4H_2O$ (Sigma Aldrich) were dissolved in 5 mL of DMF with vigorous stirring. The DMF solution was then added into the PVP/ethanol solution followed by vigorous stirring for 24 h at room temperature to form a homogeneous solution for further electrospinning.

Electrospinning of the precursor solution was carried out using a single-spinneret electrospinning setup. High voltage of 16 kV was applied between the needle tip and the aluminum foil collector placed at a distance of 15 cm, at a flow rate of 1 mL h^{-1}. For the following thermolysis process, the as-spun fiber was heated in ambient atmosphere with a heating and cooling rate of 1 °C min^{-1} and calcinated at 600 °C for 24 h, 700 °C for 5 h, and 800 °C for 5 h, respectively.

2.2. Characterization. The crystallite structures were determined by a Shimadzu X-ray diffractometer (Cu Kα) with step scanning (0.02°, 0.6 s dwell time, 40 kV) over a 2θ range of 10−80°. Fourier transform infrared (FT-IR) spectra were obtained using a Perkin-Elmer Spectrum GX instrument using KBr pellet technique at a resolution of 1 cm^{-1}. Thermogravimetric analysis (TGA, Q500) was determined from room temperature to 900 °C under a continuous air flow at 10 °C min^{-1}. The surface area analysis was recorded using Brunauer Emmett and Teller (Micromeritics, ASAP 2020). X-ray photoelectron spectroscopy (XPS) was performed with a Kratos Axis Ultra DLD electron spectrometer (PHI, PHI5300 system). The morphologies of the samples were investigated using a field emission scanning electron microscope (FESEM, JEOL JSM-7600F) at an accelerating voltage of 5 kV and transmission electron microscope and high resolution transmission electron microscope (HRTEM) (JEOL 2100F) in high resolution mode operating at 200 kV. The elemental compositions of the sample were analyzed with energy-dispersive X-ray spectroscopy (EDX) attached to the TEM instrument.

2.3. Electrochemical Measurements. Electrodes for electro-chemical studies were prepared by mixing active materials with polyvinylidene fluoride (PVDF) binder (Kynar 2801) and Super P carbon (Timcal) with weight ratios of 60:20:20, 70:15:15, and 80:10:10 in N-methylpyrrolidinone (NMP, Sigma Aldrich) to form a homogeneous slurry. The viscous slurry was coated on etched copper foil by a doctor blade (thickness ~21 μm) and dried at 80 °C in an air oven for 12 h and then pressed between twin rollers to ensure intimate contact with the current collector and cut into circular disks (16 mm diameter and containing ~3 mg active material). Due to the intrinsic electronic conducting behavior of the $CaSnO_3$ electrode, we optimized electrode composition with active material, super P carbon, and binder in a weight ratio 60:20:20 to achieve high performance composition (Figure S1, Supporting Information). The electrochemical perform-ances were investigated using CR 2016 coin cell assembled in an argon-filled glovebox with metallic lithium as a counter electrode, Celgard 2400 as the separator, and 1 M $LiPF_6$ in ethylene carbonate/diethylene carbonate (EC/DEC = 1:1, Charslton Technologies Pte Ltd.) as the electrolyte. The Galvanostatic discharge−charge cycling and cyclic voltammetry (CV) were measured using multichannel battery tester systems (Neware) and Solartron 1470E, respectively, at room temperature. Electrochemical impedance spectroscopy (EIS) measurement was carried out in the frequency range of 100 kHz to 0.1 Hz by applying 10 mV bias voltage. The data were recorded as the Nyquist plots −Z″ vs Z′, which could be analyzed using Zplot and Zview software (version 2.2, Scribner Associates Inc., U.S.A.).

3. RESULTS AND DISCUSSION

3.1. Structure and Morphology Analysis. The crystalline structure, composition, and phase purity of the electrospun products calcined at different temperatures were first investigated by XRD, as shown in Figure 1. For the sample calcined at 600 °C for 5 h, all the peaks correspond to SnO_2 phase (JCPDS 41-1445) and $CaSnO_3$ phase cannot be observed. This indicates that Ca^{2+} could not be effectively
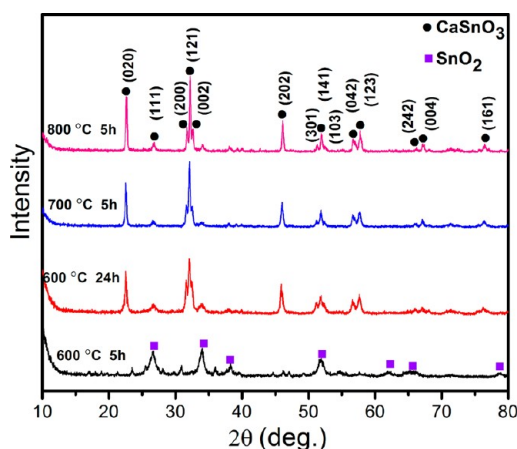
Figure 1. XRD patterns of $CaSnO_3$ calcinated at different temperatures and times.

built into the lattice under this condition. Increasing calcination duration to 24 h (at 600 °C) resulted in formation of perovskite $CaSnO_3$ structure (JCPDS 31-0312, SG: P212121 (19), a_0 = 5.6615 Å, b_0 = 7.8825 Å, c_0 = 5.5162 Å).[38] No secondary impurity phase was found, indicating single-phase $CaSnO_3$ formation. As expected, after calcinating at 700 and 800 °C for 5 h, respectively, the obtained products are pure $CaSnO_3$ and all diffraction peaks increase in intensity with increasing calcination temperature due to an increase of crystallinity. The XRD result is also supported by thermogravimetric analysis (Figure S2, Supporting Information). A weight loss of about 11% before 200 °C is assigned to the volatile solvent, absorbed moisture, and crystal water in the metallic precursor. A large weight loss of about 67% can be attributed to the removal of PVP and the decomposition of metallic precursor. Above 600 °C, no more weight loss occurs, indicating the complete removal of organic species, and hence, the calcination temperatures of 600, 700, and 800 °C were employed.

FT-IR spectra of the PVP precursor, as-spun nanofibers, and calcined $CaSnO_3$ at 700 °C for 5 h are shown in Figure 2,
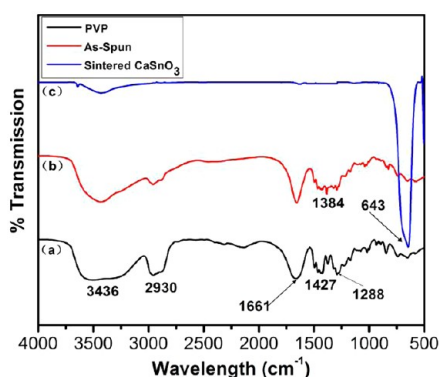

Figure 2. FT-IR spectra of (a) PVP, (b) as-spun nanofibers, and (c) calcinated $CaSnO_3$ at 700 °C for 5 h.

respectively. The broad absorption band observed at 3436 cm^{-1} can be ascribed to the symmetric stretching vibration of −OH groups, owing to the presence of adsorbed moisture and ethanol solvent. The peaks at 2930 and 1427 cm^{-1} can be assigned to the symmetric stretching and bending of C−H group due to the presence of PVP. The characteristic peaks centered at about 1661 cm^{-1} correspond to the C=O

functional group of PVP. The peaks at around 1288 cm^{-1} can be interpreted as the absorption of tertiary amine group of PVP.[39] The peaks of the as-spun nanofibers are similar to the PVP precursor except for new peaks that appeared at around 1384 cm^{-1}, which indicates the existence of trapped ethanol solvent. After calcinating at 700 °C for 5 h, the organic component peaks disappeared completely due to decomposition of PVP, while a new peak at about 643 cm^{-1} appeared that is assigned to Sn−O−Sn antisymmetric and symmetric vibrations,[40] indicating the onset of crystallization. FT-IR spectra analysis proves that the PVP has been thoroughly removed by calcination and pure phase of $CaSnO_3$ nanocrystallites formed.

The chemical composition and surface valence states of the $CaSnO_3$ obtained at 700 °C were investigated by XPS, as shown in Figure 3. The characterization of lithium ion batteries

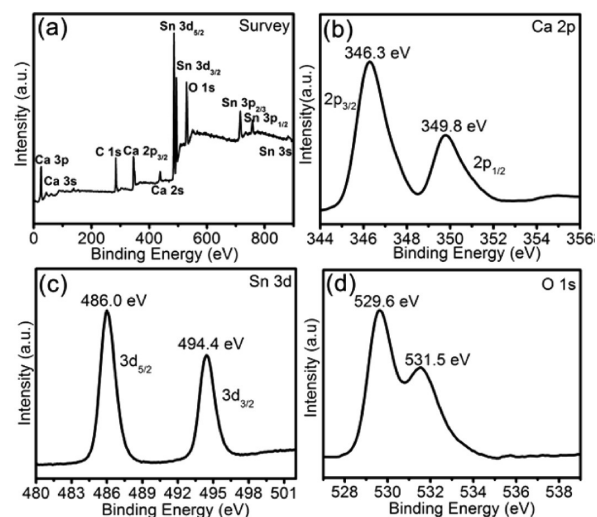**Figure 3.** XPS pattern of $CaSnO_3$ calcinated at 700 °C for 5 h (a) survey scan, (b) high resolution Ca 2p scan, (c) high resolution Sn 3d scan, and (d) high resolution O 1s scan.

materials and other oxides extensively use XPS to evaluate the valence states of the metal/nonmetal ions. The survey XPS spectrum (Figure 3a) clearly reveals that mainly Ca, Sn, and O elements exist along with adventitious carbon. There are doublet peaks with binding energy (BE) at 346.3 and 349.8 eV (Figure 3b), which correspond to Ca $2p_{3/2}$ and $2p_{1/2}$ spin−orbit splitting peaks with a BE separation of 3.5 eV, respectively. This result is in good agreement with BE values reported in the literature.[25] The Sn 3d spectrum shows BEs of 486.0 and 494.4 eV for $3d_{5/2}$ and $3d_{3/2}$, respectively (Figure 3c). The BE separation of Sn 3d spectra is 8.4 eV. All of these clearly indicate that Ca and Sn have +2 and +4 oxidation states in $CaSnO_3$. The BE of O1s spectra at 529.6 and 531.5 eV can be assigned to the lattice oxygen and adsorbed oxygen (Figure 3d). Furthermore, the quantification of XPS spectra give the atom ratio of Ca/Sn/O of 19.58%:19.93%:60.49%, which is almost in agreement with the stoichiometry of $CaSnO_3$. The XPS study is consistent with our XRD and FT-IR results, indicating formation of pure single phase $CaSnO_3$ under such conditions.

To elucidate the morphologies and microstructures of the metal oxide fibers calcinated at different temperatures from 600 to 800 °C, FESEM and HRTEM were carried out, as shown in Figures 4, 5, and 6. It is worth pointing out that the

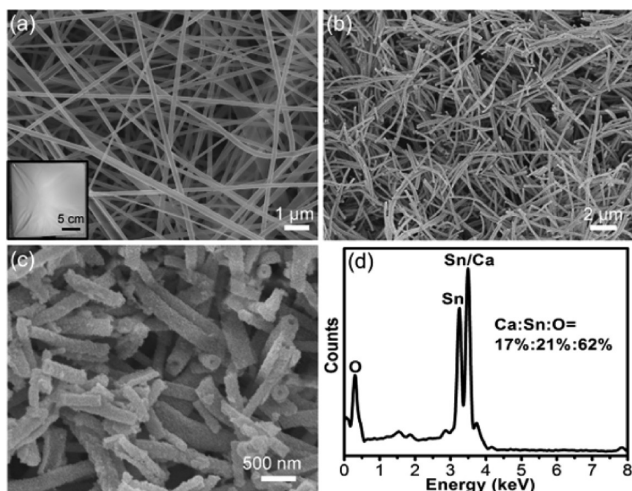**Figure 4.** FESEM images of (a) as-spun nanofibers and (b, c) calcinated $CaSnO_3$ at 700 °C for 5 h; (d) EDX spectra of calcinated $CaSnO_3$ at 700 °C for 5 h. The inset is the photo of the electrospun precursor film.
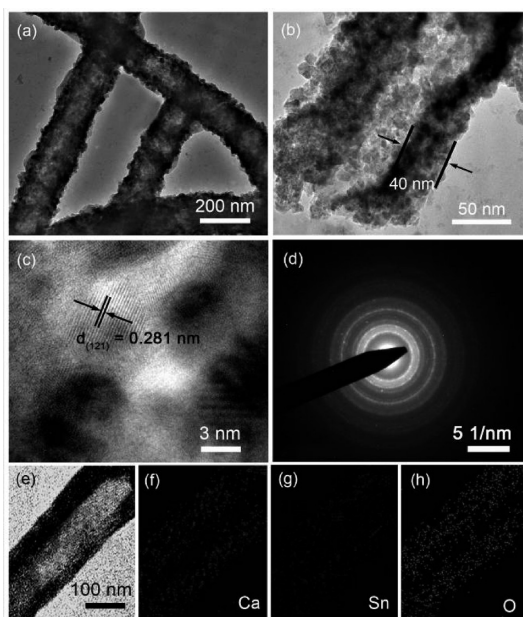

Figure 5. (a−c) TEM and HRTEM images of calcinated $CaSnO_3$ at 700 °C for 5 h, (d) the corresponding SAED pattern, and (e−h) TEM image and the corresponding EDX elemental mappings of Ca, Sn, and O (as labeled) for calcinated $CaSnO_3$ at 700 °C for 5 h.

Figure 6. FESEM images (left) and corresponding high-magnification of FESEM images (right) calcinated $CaSnO_3$ at (a, b) 600 °C for 24 h and (c, d) 800 °C for 5 h. TEM and corresponding HRTEM images (inset) of calcinated $CaSnO_3$ at (e) 600 °C for 24 h and (f) 800 °C for 5 h.

morphology and diameter of 1D nanomaterials prepared by electrospinning are tuned by processing parameters and will have an influence on the performance of the final products.[32,37] By adjusting some of the electrospun parameters such as the applied voltage, the ratio of inorganic salt in solution, and the feeding rate of electrospun solution, we obtain continuous nanofibers with uniform diameter of ~250 nm and smooth surface, as shown in Figure 4a. Furthermore, the obtained electrospun products can form films on aluminum substrate and are easy to collect (inset in Figure 4a). In order to study the electrochemical performance of pure 1D inorganic nanomaterial $CaSnO_3$, a high temperature calcinating process is employed to eliminate PVP. It is noted that the as-spun nanofibers turn into nanotubes after calcinating at 700 °C for 5
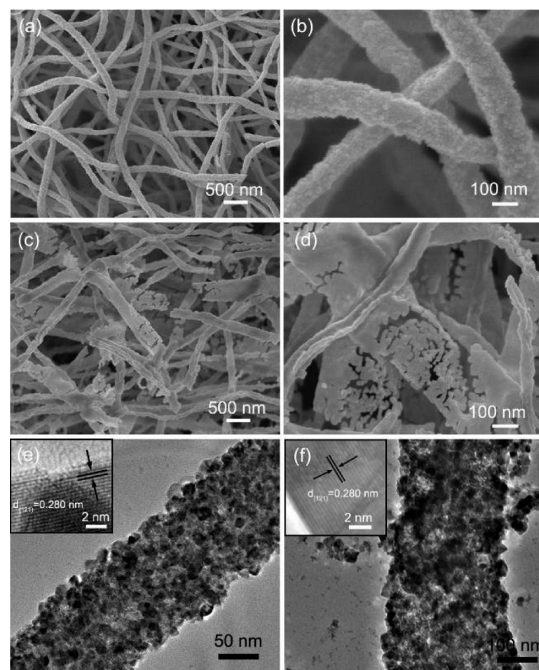
h. Figure 4b,c clearly presents the tube-like morphology. Furthermore, the surface of $CaSnO_3$ nanotubes become rough, and the average diameter of $CaSnO_3$ nanotubes is reduced to about ~180 nm due to the decomposition of PVP and the formation of inorganic phase $CaSnO_3$. The EDX was used to analyze the elemental composition of $CaSnO_3$ nanotubes, as shown in Figure 4d. Strong signals indexed to Ca, Sn, and O were presented, further indicating the formation of $CaSnO_3$ in 1D nanostructure. Therefore, the above results confirm the formation of nanocrystalline $CaSnO_3$ nanotubes, matching well with the SEM and XRD results.

The crystalline structures of $CaSnO_3$ nanotubes were further confirmed by TEM and HRTEM. Figure 5a,b clearly exhibits the tube-like morphology of $CaSnO_3$ nanotubes, which consisted of individual nanocrystallites with a crystallite size of ~10 nm. It can be observed that the edge and middle part of nanotubes show different color, which corresponded to the wall (~40 nm) and interior hollow structure (~90 nm), respectively. HRTEM images of $CaSnO_3$ nanotubes (Figure 5c) clearly show well-resolved lattice fringes with interplanar spacing of ~0.281 nm that correspond to the (121) plane of $CaSnO_3$, agreeing well with the d (121) spacing of the literature value (0.2789 nm) (JCPDS 31-0312). The SAED pattern of $CaSnO_3$ nanotubes show diffraction rings (Figure 5d), indicating the polycrystalline nature of the $CaSnO_3$ nanotubes. The composition distribution of $CaSnO_3$ nanotubes is further identified by EDX elemental mapping. Figure 5f−h presents the even distribution of Ca, Sn, and O, and the same tube-like shape is exhibited exactly as it is observed under TEM (Figure 5e). The results support the tube-like structure as well.

As we all know, the calcination temperature has a dramatic effect on both the morphology and size of the product in the present synthesis. For example, the conventional electrospun fiber morphology of $CaSnO_3$ nanofibers has been maintained

after calcination at 600 °C for 24 h (Figure 6a, b). The average diameter of CaSnO$_3$ nanofibers is about ~150 nm, which is smaller than that of CaSnO$_3$ nanotubes. The TEM images of CaSnO$_3$ nanofibers calcined at 600 °C for 24 h (Figure 6e) reveal that nanocrystals formed the interconnected fibrous morphology, which is consistent with the SEM result. CaSnO$_3$ phase can be identified in the corresponding HRTEM image inset in Figure 6e. However, the 1D CaSnO$_3$ materials crack at 800 °C for 5 h and ultimately present ruptured nanobelts, as shown in Figure 6c,d. Similarly, the ruptured nanobelt morphology of CaSnO$_3$ calcinated at 800 °C for 5 h is further confirmed by TEM, as shown in Figure 6f. Furthermore, the nanoparticles around the nanobelts in Figure 6f demonstrated the rupture of nanobelts. Again, the corresponding HRTEM image (Figure 6f, inset) supports that CaSnO$_3$ phase has formed.

3.2. Formation Mechanism. It is worth to point out that the morphologies such as nanofibers or nanotubes are largely dependent on the calcination temperature. The high calcination temperature is favorable for creating spaces among the nanocrystals. These factors should be controlled under an appropriate range; too high or too low will influence the morphology of products. The formation mechanism of electrospun CaSnO$_3$ nanotubes is similar to that of the spray drying of ceramic powders.[41] During the calcination process, PVP was gradually removed with the increase of temperature. A variety of gases are produced such as carbon oxides, gaseous solvent molecules, and other gases due to the decomposition of PVP and solvent evaporation. Thus, this leads to the internal and external pressure difference of the fibers and the ballooning of the fiber occurs. Furthermore, CaSnO$_3$ primary nanocrystals first formed in the precursor fibers in both outside and inner sites. Whether hollow structures can be formed or not is determined by many factors such as composition of fibers, the evaporating rate, and the diffusion rate of gases and CaSnO$_3$ nanograins. At a relatively lower temperature of 600 °C, the reaction rate on the outside is larger than that in the inner due to thermal unbalance, while the concentration gradient difference between the outside and inner sites is not large enough and the pressure outside of the fiber is larger than the inside pressure, owing to the diffusion rate of gases through the fiber surface larger than the evaporating rate of gases inside the fibers, finally leading to the constriction of the outside nanocrystals and formation CaSnO$_3$ nanofibers. When the calcination temperature is further enhanced to 700 °C, the reaction rate and the evaporation rate of gases in the inner sites rapidly increased. In this case, the inner nanocrystals expanded due to large strain strength, and the pressure inside of the fiber was larger than the outside pressure, resulting in the formation of CaSnO$_3$ nanotubes, as shown in the scheme 1. With further increase of the temperature to 800 °C, the nanotube structure ultimately cracked to form ruptured nanobelts.

3.3. Electrochemical Studies. The effect of morphologies on the electrochemical performance of CaSnO$_3$ as anode materials for LIBs were further evaluated. It is well-known that the electrochemical performance of LIBs is highly dependent on the voltage window and current rate.[42,43] A wider window creates harsher conditions for the insertion/extraction of lithium. Therefore, a wider voltage window of 0.005−3.0 V was applied in this study. The cyclabilities of CaSnO$_3$ calcinated at different conditions were compared and shown in Figure 7a. CaSnO$_3$ nanotubes manifest enhanced capacity retention as compared to the two counterparts. Specifically, after 50 cycles, a

Scheme 1. Schematic Illustration for the Formation Process of the CaSnO$_3$ Nanofibers, Nanotubes, and Ruptured Nanobelts
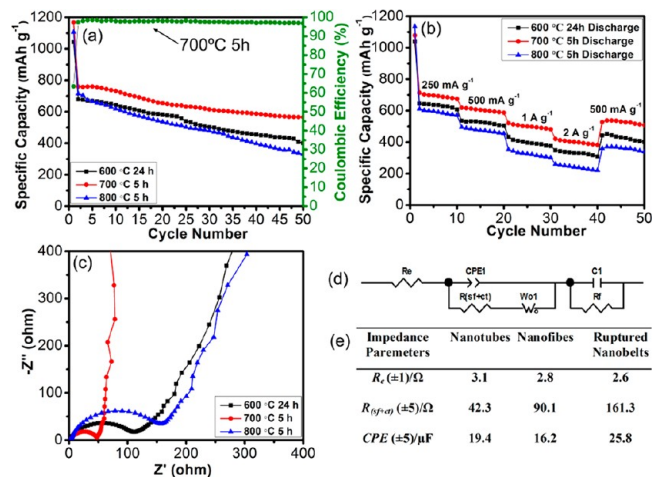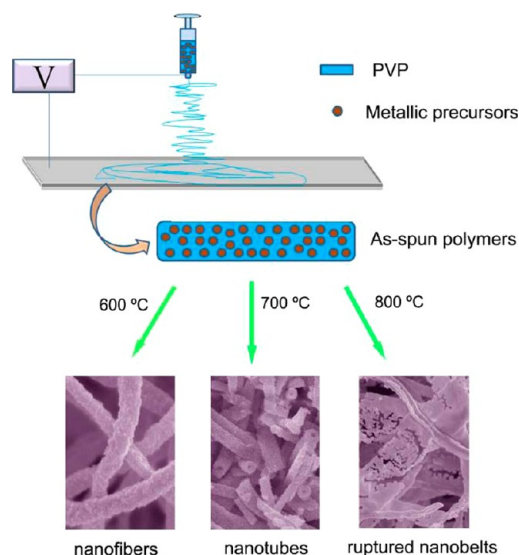

Figure 7. (a) Capacity and Coulombic efficiency versus cycle number of the electrospun CaSnO$_3$ nanomaterials (current density = 60 mA g^{-1}). (b) Capacity versus cycle number of CaSnO$_3$ nanomaterials at different current density. (c) Nyquist plots for CaSnO$_3$ nanomaterials. (d) The equivalent circuit which is used to fit the experimental date. R is the electrolyte resistance; IP is the interparticle resistance. CPE is constant phase elements, and W is the Warburg impedance; C_1 is the intercalation capacitance. (e) Fitted impedance parameters obtained from EIS data using the circuit in (d).

higher reversible capacity of 565 mAh g^{-1} is delivered by CaSnO$_3$ nanotubes, compared to 401 mAh g^{-1} for CaSnO$_3$ nanofibers and 330 mAh g^{-1} for CaSnO$_3$ ruptured nanobelts. Moreover, the Coulombic efficiency of CaSnO$_3$ nanotubes remains at about 97.5% after the second cycle. In addition, it is found that the sample calcined at 600 °C for 5 h possesses a poorer Li ion discharge/charge cycle stability than CaSnO$_3$ nanotubes (Figure S3, Supporting Information). The FESEM image reveals that the sample also possesses the fibrous morphology (Figure S3, Supporting Information). Here, the better cycling performance of the CaSnO$_3$ nanotubes is possibly related to the interior hollow tubular structure, which could effectively accommodate the large volume change

6009

dx.doi.org/10.1021/am301664e | ACS Appl. Mater. Interfaces 2012, 4, 6005−6012

and improve cyclability. The rate capability of the $CaSnO_3$ with three different morphologies is evaluated at various current rates (Figure 7b). $CaSnO_3$ nanotubes show the best rate performance compared with the two counterparts at all current densities due to the reduced lithium ion diffusion length and increased surface area of the $CaSnO_3$ nanotubes (Figure S4, Supporting Information). Moreover, a high capacity of about 400 mAh g^{-1} for $CaSnO_3$ nanotubes can be delivered at 2 A g^{-1}, while the capacities of $CaSnO_3$ nanofibers and $CaSnO_3$ ruptured nanobelts are only 331 and 241 mAh g^{-1}, respectively. Furthermore, $CaSnO_3$ nanotubes still can deliver a reversible capacity of 510 mAh g^{-1}, when the current is back to 500 mA g^{-1}. This indicate that $CaSnO_3$ nanotubes exhibit enhanced cyclic capacity and rate capacity especially considering a relatively wider voltage window applied in this study, which could probably be attributed to the following: (i) open continuous hollow interior that would facilitate the transport of Li$^+$ and electrolyte penetrating into the electrode material and (ii) the void interior space in $CaSnO_3$ nanotubes could effectively accommodate the drastic volume changes during the lithium alloying/dealloying process and provide a larger electrolyte/electrode effective contact surface, which could offer negligible diffusion times of ions and probably faster phase transitions. In addition, inactive matrix, which is generated in the initial discharge process, may play an important role that could effectively minimize the aggregation of active material due to even distribution in the whole phase and alleviate the mechanical stress caused by volume changes in the lithium alloying/dealloying process.

To provide a deeper insight into the effect of morphology on the electrochemical performance of $CaSnO_3$, electrochemical impedance spectroscopy (EIS) was carried out. The EIS spectra exhibits typical Nyquist plots, which consist of a high frequency semicircle (at 100 kHz–10 Hz) and a low frequency inclined line (at 10 Hz–0.1 Hz), as shown in Figure 7c. The high frequency semicircle represents surface film and charge transfer resistance of the following electrochemical and chemical reaction across the interface. As can be seen, the diameter of semicircle for the $CaSnO_3$ nanotubes has the lowest value, implying the best electrochemical performance. To quantify the experimental EIS results, the spectra was fitted with an equivalent electrical circuit (Figure 7d) consisting of a serial connection of R_e, $R_{(sf+ct)}$//CPE_1, R_f//C_1, and W_{o1}, where R_e is the electrolyte resistance, $R_{(sf+ct)}$ is the surface film and charge transfer resistance, R_f is the polarization resistance, CPE_1 is the constant phase elements which indicate the roughness, porosity, and inhomogeneity of the electrode surface, W_{o1} is the Warburg impedance, and C_1 is the intercalation capacitance. According to the impedance values and the shape of the curves, $CaSnO_3$ nanotubes exhibit the lowest value of R_{sf+ct} of 42.3 Ω, while the values of $CaSnO_3$ nanofibers and $CaSnO_3$ ruptured nanobelts are 90.1 and 161.3 Ω, respectively (Figure 7e). This implies that the open continuous hollow interior of $CaSnO_3$ nanotubes provide the pathway for charge transfer and lithium ion diffusion rapidly with ease, which leads to the excellent electrochemical performance of $CaSnO_3$ nanotubes. The EIS analysis also proves that the open continuous hollow interior nanotube structure is one important factor to improve the electrochemical performance of $CaSnO_3$.

$$CaSnO_3 + 4Li^+ + 4e^- \rightarrow CaO + 2Li_2O + Sn \qquad (3)$$

$$4.4Li^+ + 4.4e^- + Sn \leftrightarrow Li_{4.4}Sn \qquad (4)$$
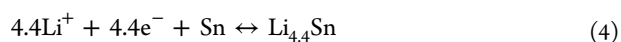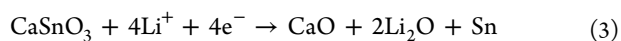
The electrochemical performance of $CaSnO_3$ nanotubes was subsequently studied. The cyclic voltammetry (CV) was carried out to clearly distinguish the electrode reaction processes, as shown in Figure 8a. The initial curve is different from the later
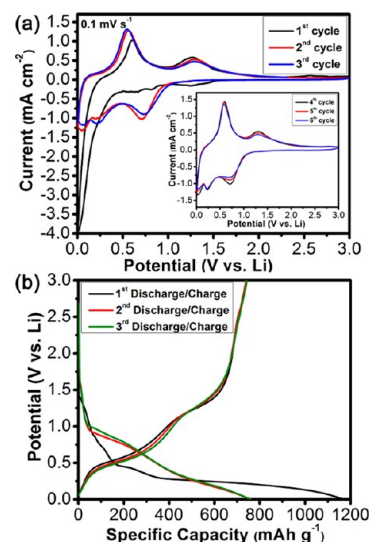

Figure 8. (a) Cyclic voltammograms of the $CaSnO_3$ nanotube electrode for the first three cycles in the voltage range of 0.005–3.0 V at scan rate of 0.1 mV s^{-1}. Scan rate of 0.1 mV s^{-1} is used from fourth to sixth (inset). (b) Discharge/charge profile of the $CaSnO_3$ nanotube electrode for the first three cycles in the voltage range of 0.005–3.0 V at the current density of 60 mA g^{-1}.

ones, while some high voltage cathodic peaks disappeared, possibly due to the formation of an inactive solid-electrolyte interface (SEI) on the surface of the active material and the structure destruction (amorphization of crystal lattice), which is the formation of electrochemically inactive CaO matrix. Therefore, in the first cycle, the cathodic peak at ~1.24 V can be assigned to the irreversible decomposition of electrolyte and Li_2O formation (eq 3), while two small cathodic peaks at ~0.8 and ~0.67 V are possibly derived from the irreversible decomposition of tin oxides to form Sn metal. Additionally, a distinct cathodic peak appears in the low voltage approaching 0 V, which can be ascribed to the reversible alloying reaction between Sn and Li. The corresponding anodic peak at ~0.58 V is observed in the CV profile. Another anodic peak at ~1.26 V may be due to the partly reversible oxidation of the tin nanoparticles to tin oxide, which means that the corresponding reduction of the tin oxide to Sn metal is occurring at ~0.60 V. In the second and third cycle, the redox couples stay rather stable at ~0.2–0.048/0.58 V and ~0.60/1.26 V. The splitting of the cathodic peak into a doublet,[24] observed at 0.2 and 0.048 V in the following cycles, is ascribed to the formation of various Li_xSn (eq 4). It should be pointed out that the anodic peak at ~0.58 V increased in intensity significantly, demonstrating a possible activation process in the electrode material. Furthermore, after the first CV cycle, the cathodic and anodic peaks overlapped very well, which indicated the remarkable reversibility of the alloying/dealloying reaction, as shown in the inset of Figure 8a.

Figure 8b describes the discharge/charge voltage profiles of $CaSnO_3$ nanotubes at a current density of 60 mA g^{-1}. The discharge/charge behavior of $CaSnO_3$ nanofibers and ruptured nanobelts for the first three cycles was also studied, and a

6010

dx.doi.org/10.1021/am301664e | ACS Appl. Mater. Interfaces 2012, 4, 6005–6012

similar mechanism was observed (Figure S5, Supporting Information), which confirmed that different morphologies make no difference on the redox reaction. Here, consistent with the above CV analysis, four voltage plateaus at ~1.24, ~0.8, ~0.67, and ~0.2 V can be identified in the first discharge process, and it deliver a very high discharge capacity of 1168 mAh g^{-1}, which is slightly higher than the theoretical value of 1089 mAh g^{-1}. This result can be ascribed to the SEI formation due to the reaction of Li with the solvents of the electrolyte. The subsequent charge process gives a charge capacity of 741 mAh g^{-1}. The initial Coulombic efficiency is around 63%, which could be attributed to the first irreversible reaction. The discharge and charge capacities in the second cycle were 759 and 739 mAh g^{-1}, respectively, resulting in an increased efficiency value of 97.3%. Moreover, the Coulombic efficiency remains at ~97.5% in the following cycles. The CaSnO$_3$ nanotubes greatly enhanced lithium storage properties.

4. CONCLUSIONS

CaSnO$_3$ nanotubes have been successfully prepared by a facile single spinneret electrospinning method. The morphologies of CaSnO$_3$ nanotubes, nanofibers, and ruptured nanobelts could be easily controlled by adjusting the calcination temperature. Electrochemical evaluation revealed that the CaSnO$_3$ nanotubes exhibited excellent cyclability and rate capability, when compared with CaSnO$_3$ nanofibers and CaSnO$_3$ ruptured nanobelts. The reversible capacity of 565 mAh g^{-1} was delivered after 50 cycles at a current density of 60 mA g^{-1}, with coulomibic efficiency of nearly 97.5%. These enhanced performances were caused by the unique interior hollow structure, which could benefit the lithiation/delithiation process. Thus, CaSnO$_3$ nanotubes will be a promising potential anode material for LIBs, and this study will be useful for understanding not only the effect of temperature on electrospun nanofibers but also the importance of preparing 1D nanostructure materials with hollow structure.

■ ASSOCIATED CONTENT

Ⓢ Supporting Information

Cycling performance of CaSnO$_3$ electrode with different compositions. BET results, TGA curve, cycling performance of calcinated CaSnO$_3$ at 600 °C for 5 h, and discharge/charge profile of CaSnO$_3$ nanofibers and CaSnO$_3$ ruptured nanobelts. This information is available free of charge via the Internet at http://pubs.acs.org/.

■ AUTHOR INFORMATION

Corresponding Author
*E-mail: madhavi@ntu.edu.sg. Fax: +65 6790 9081. Tel: +65 6790 4606.

Notes
The authors declare no competing financial interest.

■ ACKNOWLEDGMENTS

■ REFERENCES

(1) Tarascon, J. M.; Armand, M. *Nature* **2001**, *414*, 359−367.

(2) Cheng, F. Y.; Liang, J.; Tao, Z. L.; Chen, J. *Adv. Mater.* **2011**, *23*, 1695−1715.

(3) Cabana, J.; Monconduit, L.; Larcher, D.; Palacín, M. R. *Adv. Mater.* **2010**, *22*, E170−E192.

(4) Wang, Y.; Lee, J. Y. *J. Phys. Chem. B* **2004**, *108*, 17832−17837.

(5) Ahn, H. J.; Choi, H. C.; Park, K. W.; Kim, S. B.; Sung, Y. E. *J. Phys. Chem. B* **2004**, *108*, 9815−9820.

(6) Zhu, J.; Lu, Z.; Aruna, S. T.; Aurbach, D.; Gedanken, A. *Chem. Mater.* **2000**, *12*, 2557−2566.

(7) Park, M. S.; Wang, G. X.; Kang, Y. M.; Wexler, D.; Dou, S. X.; Liu, H. K. *Angew. Chem., Int. Ed.* **2007**, *46*, 750−753.

(8) Kim, H.; Cho, J. *J. Mater. Chem.* **2008**, *18*, 771−775.

(9) Guo, Z. P.; Du, G. D.; Nuli, Y.; Hassan, M. F.; Liu, H. K. *J. Mater. Chem.* **2009**, *19*, 3253−3257.

(10) Sandu, I.; Brousse, T.; Schleich, D. M.; Danot, M. *J. Solid State Chem.* **2004**, *177*, 4332−4340.

(11) Huang, F.; Yuan, Z.; Zhan, H.; Zhou, Y.; Sun, J. *Mater. Chem. Phys.* **2004**, *83*, 16−22.

(12) Ji, L.; Lin, Z.; Toprakci, O.; Zhang, X.; Khan, S. A. *ACS Appl. Mater. Interfaces* **2011**, *3*, 2534−2542.

(13) Lin, Y. S.; Duh, J. G.; Hung, M. H. *J. Phys. Chem. C* **2010**, *114*, 13136−13141.

(14) Derrien, G.; Hassoun, J.; Panero, S.; Scrosati, B. *Adv. Mater.* **2007**, *19*, 2336−2340.

(15) Chang, C. C.; Liu, S. J.; Wu, J. J.; Yang, C. H. *J. Phys. Chem. C* **2007**, *111*, 16423−16427.

(16) Belliard, F.; Irvine, J. T. S. *J. Power Sources* **2001**, *97−98*, 219−222.

(17) Becker, S. M.; Scheuermann, M.; Sepelak, V.; Eichhofer, A.; Chen, D.; Monig, R.; Ulrich, A. S.; Hahn, H.; Indris, S. *Phys. Chem. Chem. Phys.* **2011**, *13*, 19624−19631.

(18) Rong, A.; Gao, X. P.; Li, G. R.; Yan, T. Y.; Zhu, H. Y.; Qu, J. Q.; Song, D. Y. *J. Phys. Chem. B* **2006**, *110*, 14754−14760.

(19) Lei, S. J.; Tang, K. B.; Chen, C. H.; Jin, Y.; Zhou, L. *Mater. Res. Bull.* **2009**, *44*, 393−397.

(20) Wang, G.; Gao, X. P.; Shen, P. W. *J. Power Sources* **2009**, *192*, 719−723.

(21) Yuan, Z.; Huang, F.; Sun, J.; Zhou, Y. *J. Mater. Sci. Lett.* **2003**, *22*, 143−144.

(22) Huang, F.; Yuan, Z. Y.; Zhan, H.; Zhou, Y. H.; Sun, J. T. *Mater. Lett.* **2003**, *57*, 3341−3345.

(23) Hu, X.; Tang, Y.; Xiao, T.; Jiang, J.; Jia, Z.; Li, D.; Li, B.; Luo, L. *J. Phys. Chem. C* **2010**, *114*, 947−952.

(24) Sharma, Y.; Sharma, N.; Rao subba, G. V.; Chowdari, B. V. R. *Chem. Mater.* **2008**, *20*, 6829−6839.

(25) Sharma, N.; Shaju, K. M.; Rao subba, G. V.; Chowdari, B. V. R. *J. Power Sources* **2005**, *139*, 250−260.

(26) Sharma, N.; Shaju, K. M.; Rao subba, G. V.; Chowdari, B. V. R. *Electrochem. Commun.* **2002**, *4*, 947−952.

(27) Zhao, S.; Bai, Y.; Zhang, W. F. *Electrochim. Acta* **2010**, *55*, 3891−3896.

(28) He, Z. Q.; Xiong, L. Z.; Ma, M. Y.; Xiao, Z. B.; Wu, X. M.; Huang, K. L. *Chin. J. Inorg. Chem.* **2005**, *21*, 1311−1315.

(29) Mouyane, M.; Womes, M.; Jumas, J. C.; Olivier-Fourcade, J.; Lippens, P. E. *J. Solid State Chem.* **2011**, *184*, 2877−2886.

(30) Sharma, Y.; Sharma, N.; Rao subba, G. V.; Chowdari, B. V. R. *J. Power Sources* **2009**, *192*, 627−635.

(31) Bruce, P. G.; Scrosati, B.; Tarascon, J. M. *Angew. Chem., Int. Ed.* **2008**, *47*, 2930−2946.

(32) Feng, J. K.; Lai, M. O.; Lu, L. *Electrochem. Commun.* **2011**, *13*, 287−289.

(33) Wang, C.; Zhou, Y.; Ge, M.; Xu, X.; Zhang, Z.; Jiang, J. Z. *J. Am. Chem. Soc.* **2009**, *132*, 46−47.

(34) Mai, L. Q.; Xu, L.; Han, C. H.; Xu, X.; Luo, Y. Z.; Zhao, S. Y.; Zhao, Y. L. *Nano Lett.* **2010**, *10*, 4750−4755.

(35) Du, N.; Zhang, H.; Chen, B. D.; Ma, X. Y.; Yang, D. R. *Chem. Commun.* **2008**, *26*, 3028−3030.

(36) Wang, Y.; Lee, J. Y.; Zeng, H. C. *Chem. Mater.* **2005**, *17*, 3899−3903.

6011

dx.doi.org/10.1021/am301664e | *ACS Appl. Mater. Interfaces* 2012, 4, 6005−6012

(37) Li, D.; Xia, Y. *Adv. Mater.* **2004**, *16*, 1151−1170.

(38) Zhang, N.; Zhang, Z. C.; Zhou, J. G. *J. Sol-Gel Sci. Technol.* **2011**, *58*, 355−359.

(39) Cui, Q. Z.; Dong, X. T.; Wang, J. X.; Li, M. *J. Rare Earths* **2008**, *26*, 664−669.

(40) Mu, J. B.; Chen, B.; Guo, Z. C.; Zhang, M. Y.; Zhang, Z. Y.; Shao, C. L.; Liu, Y. C. *J. Colloid Interface Sci.* **2011**, *356*, 706−712.

(41) Li, G.; Hou, Z.; Peng, C.; Wang, W.; Cheng, Z.; Li, C.; Lian, H.; Lin, J. *Adv. Funct. Mater.* **2010**, *20*, 3446−3456.

(42) Lou, X. W.; Li, C. M.; Archer, L. A. *Adv. Mater.* **2009**, *21*, 2536−2539.

(43) Li, L.; Yin, X.; Liu, S.; Wang, Y.; Chen, L.; Wang, T. *Electrochem. Commun.* **2010**, *12*, 1383−1386.